

# Suppressing Dissolution of Vanadium from Cation-Disordered $\text{Li}_{2-x}\text{VO}_2\text{F}$ via a Concentrated Electrolyte Approach

Musa Ali Cambaz,<sup>†</sup> Bhaghavathi P. Vinayan,<sup>†</sup> Syed Atif Pervez,<sup>†</sup> Rune E. Johnsen,<sup>‡</sup> Holger Geßwein,<sup>§</sup> Alexander A. Guda,<sup>||</sup> Yury V. Rusalev,<sup>||</sup> Michael Kiarie Kinyanjui,<sup>⊥</sup> Ute Kaiser,<sup>⊥</sup> and Maximilian Fichtner<sup>\*,†,‡,§</sup>

<sup>†</sup>Helmholtz Institute Ulm (HIU) Electrochemical Energy Storage, Helmholtzstrasse 11, D-89081 Ulm, Germany

<sup>‡</sup>Technical University of Denmark, Department of Energy Conversion and Storage, Frederiksborgvej 399, DK-4000 Roskilde, Denmark

<sup>§</sup>Institute for Applied Materials, Karlsruhe Institute of Technology, Hermann-von-Helmholtz-Platz 1, D-76344 Eggenstein-Leopoldshafen, Germany

<sup>||</sup>The Smart Materials Research Institute, Southern Federal University, Sladkova 178/24, 344090 Rostov-on-Don, Russia

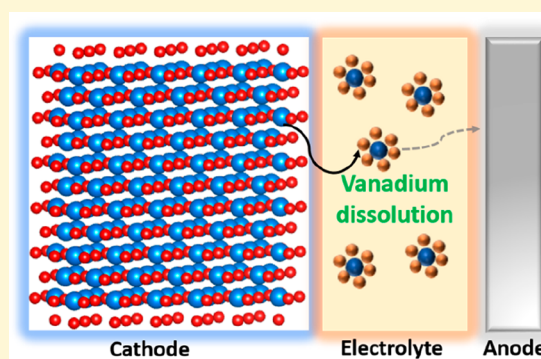
<sup>⊥</sup>Central Facility of Electron Microscopy, Ulm University, Albert Einstein Allee 11, 89068 Ulm, Germany

<sup>\*</sup>Institute of Nanotechnology, Karlsruhe Institute of Technology, D-76344 Eggenstein-Leopoldshafen, Germany

## Supporting Information

**ABSTRACT:**  $\text{Li}_2\text{VO}_2\text{F}$  with the cation-disordered rock-salt structure is an attractive high-energy-density positive electrode material but suffers from severe capacity fading upon cycling. The underlying reasons are yet unclear. In this study, we unveil the overlooked role of vanadium dissolution and electrode–electrolyte interactions and provide insight into the failure mechanism. Interfacial reactions, in general, can be tuned by either surface coatings or the modification of the electrolyte chemistry. Here we modify the interfacial reactions through the use of a concentrated electrolyte 5.5 M LiFSI in dimethyl carbonate, effectively reducing vanadium dissolution. Moreover, it results in a lower interfacial resistance build-up as compared to conventional 1.0 M  $\text{LiPF}_6$  electrolyte, thus increasing the cycling stability. The solubility of vanadium enhances significantly with higher oxidation states.

Furthermore, a chemical prelithiation strategy has been presented, which allows the full lithiation of  $\text{VO}_2\text{F}$  to  $\text{Li}_2\text{VO}_2\text{F}$ , with an outlook on the intermediate phases. We argue that the optimization of cathode–electrolyte interactions is of significant importance to improve the cycling performance of disordered rock-salts, where a thorough understanding of the limiting factors is still missing.



## INTRODUCTION

Improving the energy density of rechargeable batteries is one of the core objectives in the energy storage field. Open to debate, the positive electrode material is the bottleneck to improve the specific energy of lithium-ion batteries. State-of-the-art layered rock-salt oxides such as  $\text{LiCoO}_2$  and  $\text{LiNi}_{1/3}\text{Mn}_{1/3}\text{Co}_{1/3}\text{O}_2$  exhibit stable specific capacities between 145–165  $\text{mAh g}^{-1}$  but practically could not exceed specific capacities higher than 200  $\text{mAh g}^{-1}$  with high cycling stability.<sup>1–3</sup> With the discovery of facilitated lithium diffusion in Li-rich disordered rock-salts, this class of compound has evolved into a potential high-capacity cathode material.<sup>4</sup> This finding has opened a new perspective in the search for cathode materials showing only minor or no cation mixing. The chemical space for the cathode design, which is traditionally dominated by Ni-, Mn-, and Co-based oxides, has been broadened. Today already a large number of high capacity

positive electrode materials with disordered rock-salt structure have been reported.<sup>5–8</sup> The commonly pursued approach comprises the formation of a hypothetical solid-solution between a divalent or trivalent transition metal with a high-valent charge compensator. These include  $\text{Ti}^{4+}$ ,<sup>9</sup>  $\text{Zr}^{4+}$ ,<sup>10</sup>  $\text{Sb}^{5+}$ ,<sup>11</sup>  $\text{Nb}^{5+}$ ,<sup>12</sup> and  $\text{Mo}^{6+}$  where the transition metal is anticipated to be electrochemically inactive. Nevertheless, oxygen redox can partially reverse this penalty by contributing to the overall capacity beyond the transition metal redox capacity. This method exhibits two disadvantages: one is a heavier framework structure leading to lower specific capacity, and second, the introduced transition metal offers no redox capacity or is active in an impractical voltage window. An alternative approach is

Received: May 27, 2019

Revised: September 9, 2019

Published: September 11, 2019

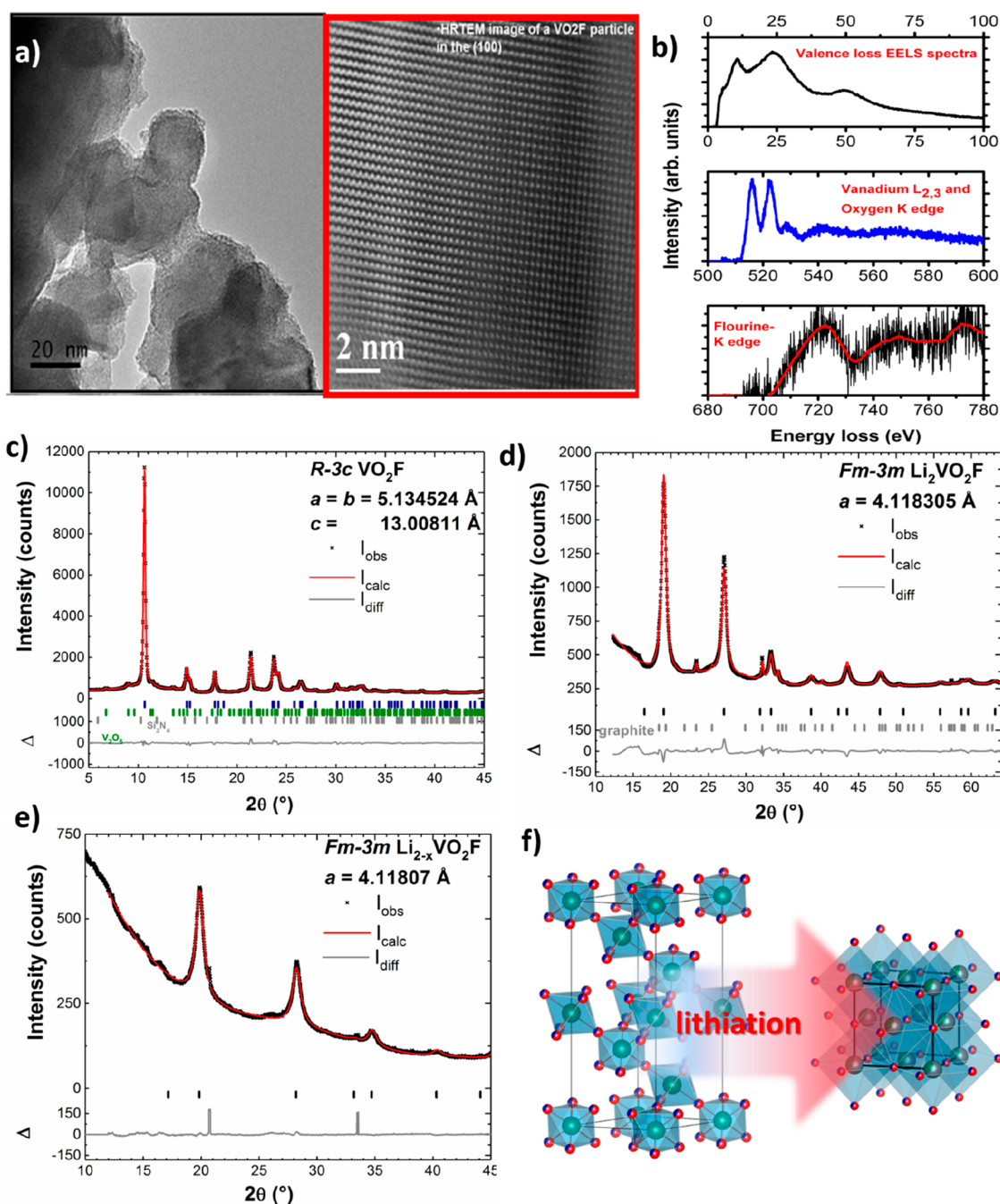


**Figure 1.** (a) HRTEM images of VO<sub>2</sub>F with an inset along the [001] zone axis. (b) EELS of VO<sub>2</sub>F with valence loss region, overlapped vanadium L<sub>2,3</sub> edge, and oxygen K-edge, fluorine K-edge. (c) Synchrotron XRPD for rhombohedral VO<sub>2</sub>F (*R*3̄*c*). (d) Synchrotron XRPD for cubic Li<sub>2</sub>VO<sub>2</sub>F (*Fm*3̄*m*) carbon composite. (e) XRPD for cubic Li<sub>2-x</sub>VO<sub>2</sub>F (*Fm*3̄*m*). (f) Schematic illustration of the crystal structures for rhombohedral VO<sub>2</sub>F and cubic Li<sub>2</sub>VO<sub>2</sub>F.<sup>30</sup>

based on the use of transition metals suitable for multiple electron transfers, such as V<sup>3+/5+</sup>,<sup>13,14</sup> Cr<sup>3+/5+</sup>,<sup>15</sup> and Mo<sup>3+/6+</sup>,<sup>16</sup> which exhibit lower average potentials. Attempts to increase the average voltage by introducing an additional transition metal with high voltage redox-couples have shown limited success. On the contrary to layered rock-salt and spinel compounds, the unusual distribution of local cation environments in disordered rock-salts gives rise to the substitution of high levels of oxygen by fluorine.<sup>17</sup> Anion substitution has been shown to increase the average voltage of these oxyfluoride materials in some cases. Hereby, the average oxidation state

decreases (for example Li<sub>2</sub>M<sup>4+</sup>O<sub>3</sub>/Li<sub>2</sub>M<sup>3+</sup>O<sub>2</sub>F), which can mitigate oxygen release by increasing the cationic charge reservoir.<sup>18</sup> Substitution of O<sup>2-</sup> with F<sup>-</sup> can be used to introduce lithium-excess (for example LiM<sup>3+</sup>O<sub>2</sub>/Li<sub>2</sub>M<sup>3+</sup>O<sub>2</sub>F) as an alternative approach to the conventional high-valent doping with heavy, redox-inactive elements and therefore offers higher theoretical capacities. Although new materials and design concepts have been introduced, high cycling stability with minor capacity fading has yet to be demonstrated. In order to avoid oxygen redox with irreversible O<sub>2</sub> gas release,

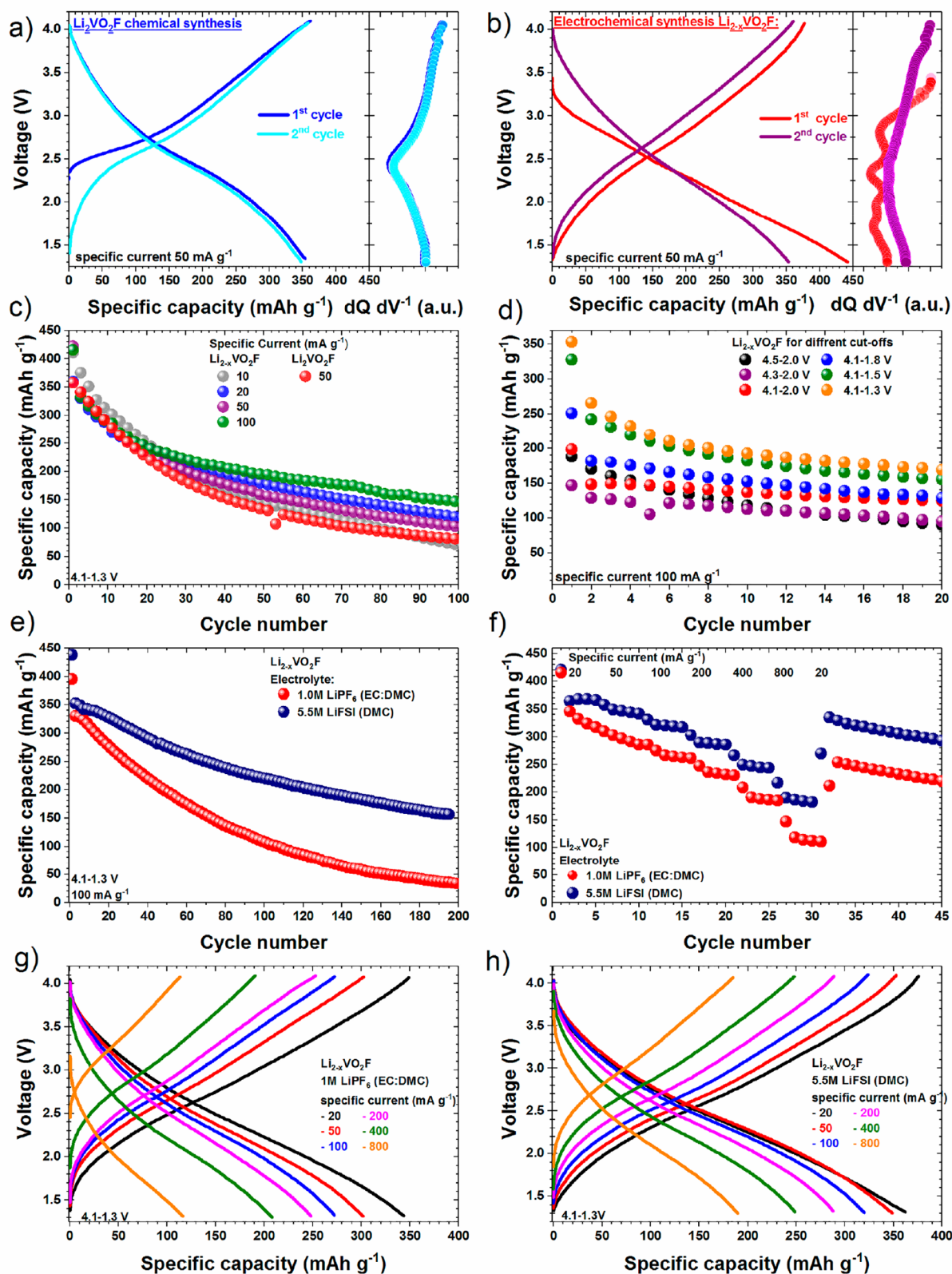


**Figure 2.** Cycling measurements were conducted in the voltage between 4.1 and 1.3 V unless stated otherwise. Charge–discharge profile of (a)  $\text{Li}_2\text{VO}_2\text{F}$  and (b)  $\text{Li}_{2-x}\text{VO}_2\text{F}$  at  $20 \text{ mA g}^{-1}$  with corresponding  $\text{dQ dV}^{-1}$ . (c) Cycling stability for various specific currents. (d) Cycling stability of  $\text{Li}_{2-x}\text{VO}_2\text{F}$  for different cut-offs. (e) Cycling stability of  $\text{Li}_{2-x}\text{VO}_2\text{F}$  at  $100 \text{ mA g}^{-1}$  for 1.0M-LiPF<sub>6</sub> and 5.5M-LiFSI. (f) Rate capability test for  $\text{Li}_{2-x}\text{VO}_2\text{F}$  for 1.0M-LiPF<sub>6</sub> and 5.5M-LiFSI. Respective charge–discharge profile from rate capability test at different specific currents for (g) 1.0M-LiPF<sub>6</sub> and (h) 5.5M-LiFSI.



maximizing the transition metal redox by employing elements capable of multielectron transfers is promising.

$\text{Li}_2\text{VO}_2\text{F}$  with a disordered rock-salt structure has a theoretical capacity of  $462 \text{ mAh g}^{-1}$  based on a 2 electron reaction ( $\text{V}^{3+/5+}$  redox reaction).<sup>13,14,19–21</sup> The thermal instability of  $\text{Li}_2\text{VO}_2\text{F}$  (decomposition  $>250^\circ\text{C}$ ) imposes challenges in the synthesis and modification of the material.<sup>19</sup>  $\text{Li}_2\text{VO}_2\text{F}$  has been synthesized by a direct mechanochemical synthesis route and through electrochemical lithiation of rhombohedral  $\text{VO}_2\text{F}$  perovskite accompanied by an irreversible phase transition to the cubic disordered rock-salt  $\text{Li}_{2-x}\text{VO}_2\text{F}$  end phase.  $\text{Li}_2\text{VO}_2\text{F}$  is an attractive high-energy-density positive electrode material, but according to recent reports<sup>21,22</sup> suffers from severe capacity fading upon cycling. The reasons for the capacity fade were still unclear. In our earlier work on  $\text{VO}_2\text{F}$ ,<sup>13</sup> vanadium deposition was found on the anode and suspected to be a source for capacity degradation. There are a variety of possible side reactions of positive electrode materials including acid–base interactions with HF and  $\text{PF}_5$  (strong Lewis acid), which are inevitably present or were formed with  $\text{LiPF}_6$  electrolytes, can lead to metal dissolution.<sup>23</sup>  $\text{LiFSI}$  salt is chemically more stable as compared to conventional  $\text{LiPF}_6$  and promises to alleviate these side reactions.<sup>24</sup>

In this work, we focus our efforts on the critical aspect of the electrode–electrolyte interaction of  $\text{Li}_{2-x}\text{VO}_2\text{F}$ , in order to better understand the degradation mechanism and the influence of the electrolyte thereof. We have used a concentrated 5.5 M  $\text{LiFSI}$  dimethyl carbonate (DMC) electrolyte (1:2.16 molar ratio salt to solvent)<sup>25,26</sup> and compared it to standard 1 M  $\text{LiPF}_6$  in DMC and ethylene carbonate (EC) electrolyte. The influence of the electrolyte on the cycling performance of  $\text{Li}_{2-x}\text{VO}_2\text{F}$  has been elaborated. X-ray photoelectron spectroscopy (XPS) and electrochemical impedance spectroscopy (EIS) were used in order to chemically and electrochemically analyze the interfaces of the electrodes. Complementary to XPS, Raman mapping was conducted at the anode side to investigate and map the metal deposition. The dissolution of vanadium from the positive electrode for both electrolytes was compared and quantified for different states of charges. Structural changes and the charge-compensation mechanism was investigated by X-ray diffraction and absorption methods. Evolving gaseous products during cycling were investigated by differential electrochemical mass spectrometry (DEMS).

## ■ RESULTS AND DISCUSSION

**Synthesis and Characterization.** For the electrochemical lithiation of  $\text{VO}_2\text{F}$  to  $\text{Li}_{2-x}\text{VO}_2\text{F}$ , cells have been constructed and then discharged to 1.3 V versus  $\text{Li}/\text{Li}^+$  at  $20 \text{ mA g}^{-1}$  current, exhibiting a discharge capacity of  $450 \text{ mAh g}^{-1}$ , which corresponds to 1.7 Li per formula unit (f.u.). The synthesis of  $R3c$   $\text{VO}_2\text{F}$  has been adopted from our previous work.<sup>13</sup> In the literature,<sup>21</sup> the electrochemical lithiation up to 1.75 Li per f.u. has been reported for the first discharge, similarly to our finding of 1.7 Li per f.u. Hence, the question about the ability to reach full lithiation remained. Here we show the accessibility up to 2 Li per f.u. is possible by chemical lithiation with the reducing agent *n*-butyllithium ( $n\text{BuLi}$ ) with a relative reduction potential of  $\sim 1.0 \text{ V}$  vs  $\text{Li}^+/\text{Li}^0$ .<sup>27</sup> The electrochemically synthesized compound is denoted by  $\text{Li}_{2-x}\text{VO}_2\text{F}$  due to the off-stoichiometry, and the chemically synthesized is denoted by  $\text{Li}_2\text{VO}_2\text{F}$ . The high-resolution transmission electron

microscopy (HRTEM) image of  $\text{VO}_2\text{F}$  along the  $[001]$  zone axis with an overview is shown in Figure 1a and reveals the typical morphology for mechanochemically synthesized compounds, showing larger agglomerated particles composed of smaller grains.<sup>28,29</sup> The individual particles are in the range of 20–50 nm. All elements V, O, and F are present, with the vanadium being in the +5 oxidation state, as shown by electron energy loss spectroscopy (EELS) in Figure 1b. The XRPD pattern of the pristine  $\text{VO}_2\text{F}$  with a rhombohedral structure (space group  $R3c$ ) is presented in Figure 1c. The refined lattice parameters are  $a = b = 5.1345(3) \text{ \AA}$ ,  $c = 13.008(1) \text{ \AA}$  and volume  $V = 296.99(4) \text{ \AA}^3$ . The X-ray powder diffraction (XRPD) of  $\text{Li}_2\text{VO}_2\text{F}$  and  $\text{Li}_{2-x}\text{VO}_2\text{F}$  are shown in Figures 1d, e, respectively. Both compounds are refined in the cubic disordered rock-salt-type structure with the  $Fm\bar{3}m$  space group. The refined lattice parameter for  $\text{Li}_2\text{VO}_2\text{F}$  is  $a = 4.1183(6) \text{ \AA}$ , and that for  $\text{Li}_{2-x}\text{VO}_2\text{F}$  is  $a = 4.1180(26) \text{ \AA}$ . The lattice parameters deviate slightly due to the differences in composition. Figure 1f shows the schematic transition of the crystal structure from the rhombohedral  $\text{VO}_2\text{F}$  to the cubic  $\text{Li}_2\text{VO}_2\text{F}$ . In the case of the chemically lithiated  $\text{Li}_{2-x}\text{VO}_2\text{F}$ , a 12 h immersion time led to a mixture of intermediate hexagonal phases and the cubic cation-disordered phase, which is shown in Figure S1 and the lattice parameter are given in Table S1.

**Electrochemistry.** We compared the electrochemical properties of  $\text{Li}_2\text{VO}_2\text{F}$  and  $\text{Li}_{2-x}\text{VO}_2\text{F}$ . The compounds were tested in the voltage range of 1.3–4.1 V at  $20 \text{ mA g}^{-1}$  current density. It is important to note that a  $2e^-$  transfer corresponds to a specific capacity of  $463 \text{ mAh g}^{-1}$  for  $\text{Li}_2\text{VO}_2\text{F}$  and to  $526 \text{ mAh g}^{-1}$  for  $\text{VO}_2\text{F}$  ( $\text{Li}_{2-x}\text{VO}_2\text{F}$ ) due to the lighter framework. For the first discharge,  $\text{Li}_2\text{VO}_2\text{F}$  exhibited a specific capacity of  $355 \text{ mAh g}^{-1}$  (1.53 Li per f.u.) with a sloping voltage profile, as shown in Figure 2a. The corresponding differential capacity versus voltage plots shows a broad peak centered at 2.5 V. Figure 2b shows the first discharge of  $\text{VO}_2\text{F}$ , exhibiting a specific capacity of  $440 \text{ mAh g}^{-1}$  (1.67 Li per f.u.). The first cycle shows a comparably high irreversible capacity, which we observed already in our previous work on the delithiation of rhombohedral  $\text{Li}_x\text{VO}_2\text{F}$ .<sup>13</sup> A closer look at the corresponding differential capacity ( $dQ/dV^{-1}$ ) versus  $V$  plot shows several peaks for the first discharge but only one peak for the consecutive cycles. This can be attributed to the irreversible, rhombohedral to cubic phase transition during the first cycle. For the second cycle, both compounds show a similar sloping voltage profile centered at  $\sim 2.5 \text{ V}$ , indicating the chemical similarity of both compounds. Figure 2c shows the cycling stability for different specific currents at 10, 20, 50, and  $100 \text{ mA g}^{-1}$  for  $\text{Li}_{2-x}\text{VO}_2\text{F}$  and at  $50 \text{ mA g}^{-1}$  for  $\text{Li}_2\text{VO}_2\text{F}$ .  $\text{Li}_{2-x}\text{VO}_2\text{F}$  shows for the same current density better cycling stability. It is noteworthy that the capacity retention is lower for slower cycling and increases with the current density. This could hint at a chemical instability of the material when in contact with the electrolyte, as lower rates mean longer contact times. Figure 2d shows the cycling stability for various cutoff voltages at  $100 \text{ mAh g}^{-1}$ . The voltage window limits the governing redox reactions and, therefore, the amount of inserted/extracted lithium. The voltage window has been varied systematically by fixing either the upper cutoff to 4.1 V or the lower cutoff to 2.0 V and gradually changing the window. In this respect, lowering the cutoff increases the specific discharge capacity drastically due to the sloping profile. On the contrary, increasing the upper cutoff from 4.1 to 4.5 V

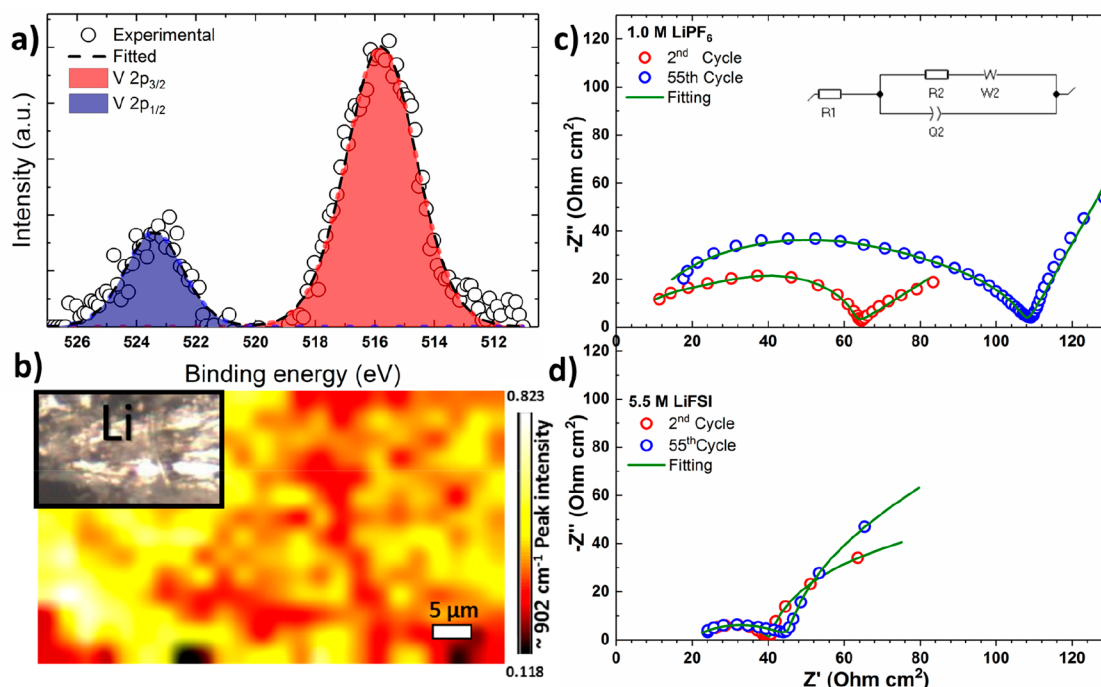


**Figure 3.** (a) XPS V 2p core level of the vanadium deposited on the anode. (b) Raman spectral imaging of  $\text{VO}_x$  thin films formed on the cycled lithium anode surface. EIS measurements on the positive electrode for different cycles. (c) 1.0M- $\text{LiPF}_6$ . (d) 5.5M- $\text{LiFSI}$ .

also enhances the capacity fading. The capacity retention decreases for higher cut-offs ( $>4.1$  V) and slower cycling, which indicates possible side reactions and instabilities of the electrode–electrolyte interface.<sup>31</sup> Finally, a concentrated 5.5 M lithium bis(fluorosulfonyl) imide ( $\text{LiFSI}$ ) in dimethyl carbonate electrolyte<sup>32</sup> was used and compared to a conventional 1.0 M  $\text{LiPF}_6$  in ethylene carbonate and dimethyl carbonate (1:1 w/w) electrolyte. Hereafter we will use the notation 5.5M- $\text{LiFSI}$  and 1.0M- $\text{LiPF}_6$ , respectively. The cycling stability has been studied at a specific current of  $100 \text{ mA g}^{-1}$  in the cycling window between 4.1 and 1.3 V, as shown in Figure 2e. For both electrolytes high irreversible capacity was observed for the first cycle. For the cells with 5.5M- $\text{LiFSI}$ , the cycling stability increased significantly, exhibiting a specific capacity of  $155 \text{ mAh g}^{-1}$  after 200 cycles compared to the cells with 1.0M- $\text{LiPF}_6$  electrolyte exhibiting only  $30 \text{ mAh g}^{-1}$ . Figure 2f illustrates the rate performance with both electrolytes, which involved five consecutive cycles at a constant specific current at 20, 50, 100, 200, 400, and  $800 \text{ mA g}^{-1}$ . The cells with 1.0M- $\text{LiPF}_6$  exhibited a capacity of 345, 302, 275, 248, 208, and  $117 \text{ mAh g}^{-1}$  for the second cycle of each current step. For 5.5M- $\text{LiFSI}$ , the corresponding values were 364, 349, 321, 289, 249, and  $190 \text{ mAh g}^{-1}$ . For higher cycle numbers, the discharge capacity deviates more due to comparably higher capacity fading of the cells with 1.0M- $\text{LiPF}_6$  electrolyte. Figures 2g,h show the charge–discharge profile of the second cycle of each current range from the rate-capability test. The molar ratios of solvent and salt of both electrolytes have to be considered to understand the cause for the differences. The molar ratio of solvent to salt corresponds to 13.6:1 for 1M- $\text{LiPF}_6$  and 2.16:1 for 5.5M- $\text{LiFSI}$ , which gives rise to different coordination and solvation of the ions. For the concentrated electrolyte, the ions are expected to form mostly contact ion pairs and aggregated solvate clusters, which can explain the relatively higher viscosity and can lead to a decrease

in the ionic conductivity.<sup>25,33</sup> Surprisingly, the rate capabilities are comparable for both electrolytes, which can principally be attributed to the improved electrolyte stability in terms of reduced solvent (unsolvated) availability and possible sacrificial anion reduction, which is hypothesized to lead to lowered interfacial resistances.

**Degradation Mechanism: Electrode–Electrolyte Interactions.** The results highlight the importance of the optimized electrolyte on the cycling stability of  $\text{Li}_{2-x}\text{VO}_2\text{F}$ . It is generally accepted that all positive electrode materials react with the commonly used electrolytes, which leads to possible passivation.<sup>31</sup> Complementary investigations were carried out with a focus on the electrode–electrolyte interactions at the positive electrode. The lithium electrode of an aged cell was investigated by X-ray photoelectron spectroscopy (XPS) and Raman spectroscopy. XPS was used to probe the oxidation state of the deposited vanadium on the lithium anode surface; the V 2p core level is shown in Figure 3a. The deconvolution of vanadium gives the V  $2p_{3/2}$  peak at 516.1 eV and the V  $2p_{1/2}$  peak at 523.5 eV, respectively, and indicates the +4 valence state of vanadium.<sup>34</sup> Furthermore, a surface mapping of vanadium on cycled Li has been done by Raman spectroscopy. It should be noted that Raman spectra are very sensitive to crystal symmetry, coordination geometry, and oxidation states, which make a profound analysis difficult. In the current study, we used Raman only to map the vanadium deposits on the lithium anode. Figure S2 shows the Raman spectra of a cycled Li surface together with the  $\text{V}_2\text{O}_5$  reference spectra. The spectra illustrate the deposition of an amorphous  $\text{VO}_x$ -like film on the cycled lithium surface, with the majority of vanadium in the  $\text{V}^{4+}$  oxidation state. This observation is in accordance with the XPS results. Figure 3b shows the Raman mapping of vanadium on the cycled Li surface using the intensity of the vanadium  $\sim 900 \text{ cm}^{-1}$  peak, which is the most intense peak

and mainly originates due to the stretching vibration of the vanadyl bonds.<sup>35,36</sup>

In order to understand the origins of the performance improvements for  $\text{Li}_{2-x}\text{VO}_2\text{F}$ , electrochemical impedance spectroscopy (EIS) analysis was performed on cycled cells. Furthermore, vanadium dissolution was qualitatively probed for both electrolytes. EIS was measured for the positive electrode at the discharged state after the first formation cycle and the 50th cycle using a three-electrode cell set up at 25 °C. The Nyquist plots for the positive electrode with 1.0M-LiPF<sub>6</sub> and 5.5M-LiFSI are shown in Figure 3, respectively. The Nyquist plots show a suppressed semicircle, at the high-frequency region, which can be attributed to the surface film resistance (R1) and the charge transfer resistance (R2) at the electrode–electrolyte interface. The Warburg line is attributed to the diffusion of the Li<sup>+</sup>-ions to the bulk phase (Warburg element). R1 resistances for 1.0M-LiPF<sub>6</sub> after the second cycle and 50th cycle were 4.1 Ω cm<sup>2</sup> and 6.6 Ω cm<sup>2</sup>, respectively. The corresponding R1 values for 5.5M-LiFSI were 22.1 Ω cm<sup>2</sup> and 20.9 Ω cm<sup>2</sup>, respectively. The relatively larger R1 values for 5.5M-LiFSI could be due to the high viscosity of concentrated electrolyte or as a result of a more dense surface film due to the decomposition of LiFSI salt. The charge transfer resistances R2 for 1.0M-LiPF<sub>6</sub> after the second cycle and 50th cycle were 30.5 Ω cm<sup>2</sup> and 99.2 Ω cm<sup>2</sup>, respectively. The corresponding R2 values for 5.5M-LiFSI were 17.3 Ω cm<sup>2</sup> and 23.9 Ω cm<sup>2</sup>, respectively. Remarkably, unlike the significant increase of the charge-transfer resistance by ~225% for cells with 1.0 M-LiPF<sub>6</sub>, the resistances of the cells with 5.5M-LiFSI increased only slightly by ~38%. The lower charge-transfer resistance could be due to the formation of a more conductive and stable passivation layer at the cathode–electrolyte interface.<sup>37,38</sup> Furthermore, we argue that in the case of the concentrated electrolyte, dissolution and migration of transition metal can be suppressed due to the lower quantity of unsolvated solvent molecules. The use of concentrated electrolytes with LiFSI can, therefore, increase the cycle life of  $\text{Li}_{2-x}\text{VO}_2\text{F}$ .

For the dissolution study,  $\text{VO}_2\text{F}$  and nominal “ $\text{Li}_{1.7}\text{VO}_2\text{F}$ ” have been immersed in both electrolytes for 7 days at 45 °C with an electrolyte to electrode material ratio of 50 g/L. Afterward, the amount of vanadium in the electrolyte was determined by inductively coupled plasma-optical emission spectrometry (ICP-OES), and the results are summarized in Table 1. This study gives a clear indication of vanadium dissolution from the positive electrode into the carbonate electrolytes. The pristine  $\text{VO}_2\text{F}$  shows a ~20 times higher solubility as compared to the lithiated compound in the conventional 1.0M-LiPF<sub>6</sub> electrolyte. It was found that vanadium dissolution is reduced in the concentrated 5.5M-

LiFSI electrolyte showing 3 times lower solubility as compared to 1.0 M-LiPF<sub>6</sub>.

In order to correlate the quantity between deposited vanadium on the anode and the capacity loss, cells have been cycled between 4.5 and 1.3 V at a specific current of 100 mAh g<sup>-1</sup> and analyzed after 50 cycles as shown in Table 1. After 50 cycles  $\text{Li}_{2-x}\text{VO}_2\text{F}$  cycled with 5.5 M LiFSI and 1.0M-LiPF<sub>6</sub> exhibited a discharge capacity of 277 mAh g<sup>-1</sup> and 199 mAh g<sup>-1</sup> corresponding to 63% and 50% of the initial capacity, respectively. The loss of capacity due to active material loss is significantly smaller <2% as the total capacity loss based on the measured specific capacity. Interestingly, vanadium dissolution for the cycled cells is ~6 times lower for the concentrated electrolyte. The active material loss cannot account for the capacity fading but could lead to increased interfacial reactivity and catalytic decomposition of the electrolyte, which could increase capacity fading.<sup>39</sup> The discrepancy in the ratios determined for both methods can be due to higher electrolyte reactivity at 45 °C, different contact times with the electrolyte, varying state of charge influencing the dissolution rate, and possibly differences in the cathode–electrolyte interface, which changes with cycling.<sup>40</sup> The deposited vanadium was found predominantly in the +4 oxidation states, and the dissolution was enhanced for the pristine state with the oxidation state +5; we argue that higher oxidized vanadium is more soluble in carbonate electrolytes. The values we derived must be viewed with caution as we used elevated temperatures and higher active material to electrolyte ratio as compared to test cells, which can increase dissolution but qualitatively gives the right trend. Combining the ICP-OES results and the impedance measurements, we clearly demonstrate that the concentrated LiFSI electrolyte approach was effective in lowering the positive electrode material resistance and in suppressing V dissolution. As a consequence, the cycling performance was improved significantly, but the capacity fading is still pronounced. Although nanosized material is favorable in terms of kinetics offered, it possibly can promote the surface reactivity with the electrolyte due to increased surface area. A detailed mechanistic understanding of the degradation mechanism on the recently discovered Li-rich disordered rock-salts is missing. In the literature performance degradation has been directly correlated with oxygen redox/loss and the associated surface-densification.<sup>41,42</sup> Furthermore, surface-densification can lead to the loss of the lithium-excess, disturbing the lithium percolation and impeding the Li diffusion.<sup>18</sup>

**Reaction Mechanism.** In order to elucidate the charge compensation mechanism for  $\text{Li}_{2-x}\text{VO}_2\text{F}$ , we measured V K-edge XANES for different states of charge, as shown in Figures 4a, b. The comparison of the V K-edge for  $\text{VO}_2\text{F}$  with  $\text{V}_2\text{O}_5$  reference confirms the oxidation state to be V<sup>5+</sup>.  $\text{VO}_2\text{F}$  shows a weak pre-edge peak located at 5469 eV, which originates from the transition to 3d states of vanadium hybridized with 4p in the distorted octahedral environment.<sup>43</sup> Upon discharge (lithiation) from OCV (pristine state) to 1.3 V, the absorption edge shifts to lower energies, close to the position of the reference compound  $\text{Li}_2\text{VO}_2\text{F}$  with V<sup>3+</sup> as shown in Figure 4a. This trend agrees with the observed discharge capacity, corresponding to 1.7 Li per f.u. and an oxidation state of ~3.3. With deviation from octahedral symmetry, pre-edge peak intensity typically increases. Furthermore, it depends on the number of d-electrons and is maximized for the d<sup>0</sup>-configuration.<sup>43</sup> The increase of the pre-edge intensity after

**Table 1. Dissolution of Vanadium in the Electrolyte at 45 °C for the Pristine and Discharged States**

Compounds	V dissolution %	
	1.0 M LiPF <sub>6</sub>	5.5 M LiFSI
$\text{VO}_2\text{F}$	4.49 ± 0.13	1.55 ± 0.04
$\text{Li}_{1.7}\text{VO}_2\text{F}$	0.22 ± 0.01	0.02 ± 0.01
$\text{Li}_{2-x}\text{VO}_2\text{F}$	<sup>a</sup> 3.51 ± 0.04	<sup>b</sup> 1.15 ± 0.03
V concentration on Li Anode after 50 cycles		
$\text{Li}_{2-x}\text{VO}_2\text{F}$	1.8 ± 0.10	0.30 ± 0.05

<sup>a</sup>*x* = 1.37. <sup>b</sup>*x* = 1.45 and vanadium deposit on anode after 50 cycles.



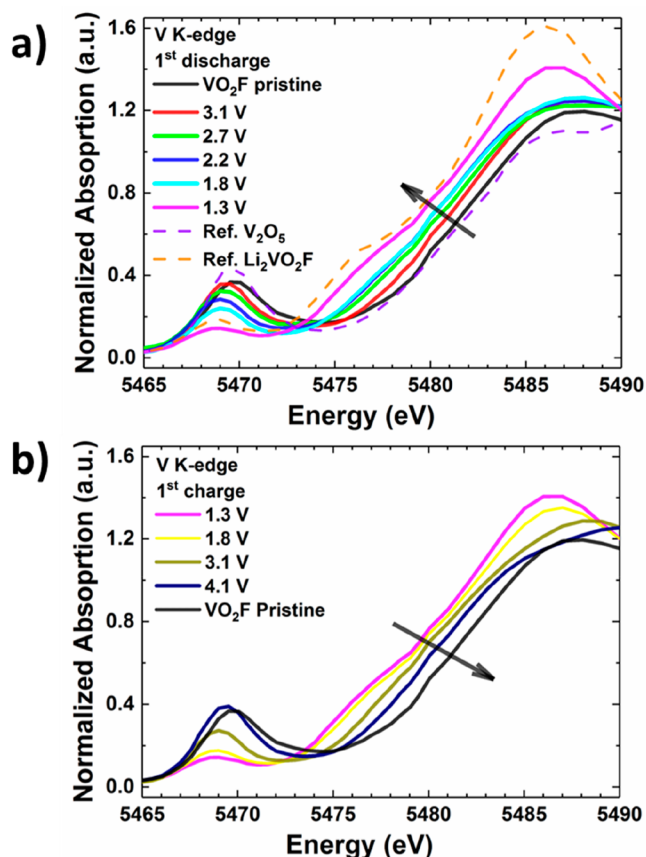


**Figure 4.** (a) V K-edge XANES for  $\text{Li}_{2-x}\text{VO}_2\text{F}$  measured at different voltages for the first discharge starting from OCV to 1.3 V. (b) V K-edge XANES measured at different voltages for the first charge.

discharge indicates a structural distortion. Upon charging, the V absorption edge shifts to higher energy values but does not recover to the edge position of the pristine  $\text{V}^{5+}$  state, as shown in Figure 4b. This observation is in accordance with the first cycle irreversibility. Recently, the first cycle irreversibility in cation-disordered oxyfluoride systems has been rationalized by the Ceder group<sup>8,44</sup> with the lithium-gettering effect introduced by fluorine (Li-rich sites around F), preferentially becoming undercoordinated for high delithiation degrees, which results in a stronger bond between Li–F and necessitates higher extraction voltages for these  $\text{Li}^+$ -ions.

*In-situ* differential electrochemical mass spectrometry (DEMS) measurements were conducted for  $\text{Li}_2\text{VO}_2\text{F}$ . The upper cutoff voltage was varied from 4.5 V in the first cycle to 4.8 V for the second and third cycles. Figure S3 compares the potential and gas evolution profiles for the first three cycles.  $\text{CO}_2$  evolution started at 3.6 V and increases along with the potential and can be attributed to the electrochemical electrolyte oxidation.<sup>45,46</sup> For the second cycle with the higher cutoff, CO evolution was observed at 4.7 V, which can possibly be attributed to the oxidation of conductive carbon.<sup>47</sup>

**Summary.** In summary, we have investigated the failure mechanism of  $\text{Li}_{2-x}\text{VO}_2\text{F}$  from the perspective of the cathode–electrolyte interactions. The cycling stability significantly improved by using a concentrated electrolyte with 5.5 M LiFSI in DMC. Vanadium dissolution is a critical issue and can be suppressed with concentrated electrolytes. In particular, the lowered vanadium solubility and the reduced interfacial resistances were found to increase the cycling stability. The

capacity loss due to the active material loss through dissolution is considerably smaller than the total capacity fading. Therefore, improvement in cycling stability can be attributed to improved cathode–electrolyte interactions. Yet, the cycling stability continuously decreases and hints toward other degradation mechanisms. V K-edge XANES results show that charge-compensation is associated with  $\text{V}^{3+}/\text{V}^{5+}$  redox reaction accounting for the measured reversible capacity. The reoxidation to  $\text{V}^{5+}$  is incomplete and leads to high first cycle irreversibility. Furthermore, we demonstrated the feasibility to synthesize  $\text{Li}_2\text{VO}_2\text{F}$  by chemical lithiation of  $\text{VO}_2\text{F}$  with *n*-BuLi. We propose vanadium dissolution and interfacial reactivity as an additional constraint for the realization of vanadium-based disordered rock-salts with high cycling stability. The presented findings are expected to benefit other systems containing transition metals prone to dissolution.

## EXPERIMENTAL SECTION

**Synthesis.**  $\text{VO}_2\text{F}$ . The synthesis procedure was adapted from our previous work.<sup>13</sup> Stoichiometric amounts of  $\text{V}_2\text{O}_5$  and  $\text{VOF}_3$  were milled with 600 rpm for 20 h using a Fritsch P6 planetary ball mill with an 80 mL silicon nitride vial and silicon nitride ball with a ball to powder ratio of 15:1.

$\text{Li}_2\text{VO}_2\text{F}$ . Chemical lithiation was carried out in a Schlenk tube under argon atmosphere in a cold bath of dry ice/acetone mixture ( $-78^\circ\text{C}$ ). To a suspension of  $\text{VO}_2\text{F}$  in dry hexane was added at once 2.1 equiv of *n*-butyllithium (2.5 M in hexane). The suspension was stirred overnight. For complete lithiation, the suspension was heated to  $50^\circ\text{C}$  and stirred for 2 more days and then filtrated and washed several times with hexane.

5.5M-LiFSI electrolyte: LiFSI (Nippon Shokubai) and DMC (BASF) with battery grade. Electrolyte solutions were prepared by mixing the appropriate quantity of LiFSI and the solvent (5.5 mol LiFSI in 1L DMC). The obtained electrolyte was a clear solution.

**Electrochemical Measurements.** Electrochemical tests were carried out in Swagelok-type cell using lithium as a counter electrode. Electrode slurries were made of 90 wt % composite and 10 wt % polyvinylidene difluoride (PVDF) binder with *N*-methyl-2-pyrrolidone (NMP) as a solvent. The composite consists of active material and Super C65 carbon black in a weight ratio of 80:20. The mixed slurry was coated on an aluminum foil by a doctor blade technique and dried at  $120^\circ\text{C}$  for 12 h under vacuum. Each working electrode (12 mm diameter) contained approximately 3 mg of active material, and Li foil was used as a counter electrode. LP30 from BASF (ethylene carbonate/dimethyl carbonate, 1:1 weight ratio with 1 M  $\text{LiPF}_6$ ) was used as the electrolyte. Temperature controlled galvanostatic charge–discharge experiments were conducted at  $25^\circ\text{C}$  in climate chambers using an Arbin electrochemical workstation.

Electrochemical impedance spectroscopy (EIS) was performed using a three-electrode PAT-Cell (EL-CELL, Germany) with Li ring as reference electrode and Li metal (18 mm) as the counter electrode. The working electrode size was 18 mm and aluminum as the current collector. The experiments were conducted using a Bio-Logic electrochemical workstation with an applied sinusoidal excitation voltage of 10 mV in the frequency range 200 kHz–0.1 Hz.

**Differential Electrochemical Mass Spectrometry (DEMS).** The *in situ* gas analysis was performed by use of differential electrochemical mass spectrometry (DEMS). The setup has been described elsewhere.<sup>46,48</sup> Custom cells with gas in- and outlets were assembled in an argon-filled glovebox. The cathodes used were 40 mm diameter with a 4 mm hole for proper gas extraction. GF/A (42 mm diameter, GE Healthcare Life Sciences, Whatman) was used as separator, 600  $\mu\text{L}$  of LP47 (1 M  $\text{LiPF}_6$  in ethylene carbonate/diethyl carbonate, 3:7 by weight, BASF SE) as electrolyte, and 600  $\mu\text{m}$ -thick Li metal foil (Albemarle Germany GmbH) with a diameter of 40 mm as counter-electrode. A constant carrier gas flow (2.5  $\text{mL}_{\text{He}}/\text{min}$ , purity 6.0) was applied during DEMS measurements for gas

extraction. The gas was analyzed via mass spectrometry (GSD 320, OmniStar Gas Analysis System, Pfeiffer Vacuum GmbH). After each run, a calibration gas of known composition was introduced to quantify the measured ion currents.

**X-ray Diffraction.** Synchrotron X-ray powder diffraction (XRPD) experiments were performed at the Swiss-Norwegian Beamline (SNBL), beamline BM01, at the European Synchrotron Radiation Facility (ESRF). The powdered samples were filled in 0.5 mm quartz capillaries and sealed with wax under an argon atmosphere. XRPD data were collected using a PILATUS 2 M area detector from DECTRIS, a sample-to-detector distance of 142.27 mm, beam size of  $0.2 \times 0.2$  mm, a wavelength of 0.68202 Å, a  $20^\circ$  rotation of the capillary, and an exposure time of 20 s. The data were converted to conventional one-dimensional powder patterns using the FIT2D software.<sup>49</sup> The electrochemically lithiated  $\text{Li}_{2-x}\text{VO}_2\text{F}$  powder sample was sealed in between polyimide foil under an argon atmosphere. Powder diffraction data was recorded on a HUBER diffractometer with a RIGAKU micro focus rotating-anode (Mo  $K\alpha_{1,2}$  radiation), a 2D collimating multilayer optic, and a PILATUS 300 K-W detector. The area detector data were converted to one-dimensional powder patterns using the pyFAI software.<sup>50</sup>

**Raman.** Raman measurements of the surface of cycled Lithium were conducted using an ECC-Opto-Std [EL-CELL GmbH] electrochemical cell. The washed lithium after battery cycling was kept at the electrode side of an ECC-Opto-Std [EL-CELL GmbH] cell and sealed with a thin optical glass window (0.15 mm) and made airtight with a rubber seal. The whole cell was fabricated inside a glovebox. The Raman spectra and mapping were acquired using an inVia confocal Raman microscope (RENISHAW) with a 532 nm laser excitation source in the spectral range 600–1000  $\text{cm}^{-1}$ . A grating was used as a dispersion element with a groove density of 2400 l/mm. The slit opening of the confocal system was fixed at 65  $\mu\text{m}$  and centered at 1859  $\mu\text{m}$ , respectively. The laser was focused on the sample using a 20 $\times$  objective. The nominal laser power was filtered down to 4 mW to avoid sample overheating. Every spectrum recorded resulted from an average of 2 acquisitions of 5 s each. The data were analyzed using inVia WiRE 4.4 Software.

**TEM.** High-resolution transmission electron microscopy (HRTEM) imaging was performed on a Titan 80-300 TEM equipped with an objective lens spherical aberration (Cs) corrector and operated at 80 kV. EELS spectra were acquired using a Gatan-Tridiem spectrometer attached to the TEM. The energy resolution was determined to be 0.60 eV. Short exposure times in the order of 0.05–0.1 s were used during the acquisition of the spectrum. The spectra were corrected for multiple scattering by using the Fourier-log deconvolution method. For the O–K V L<sub>2,3</sub> and F–K edges, the acquisition times were in the order of 5 s. The background contribution at the F–K, O–K edge, and V L<sub>2,3</sub> edges was subtracted after fitting of the background using a power law  $AE^{-r}$ , with E being the energy loss and A and r being constants. In order to remove the effects of the multiple scattering, core-loss spectra were deconvoluted with the low loss spectrum.

**XANES.** The V K-edge XANES spectra were measured with a laboratory Rigaku R-XAS spectrometer (Southern Federal University, Russia) in transmission mode at room temperature with a crystal monochromator Ge (311) at an energy resolution of 0.6 eV. The material was extracted from the electrochemical cell at different voltages and pressed into pellets. The latter was prepared in a glovebox and sealed in a transparent X-ray bag under an inert atmosphere for measurements. An argon-filled ionization chamber (300 mbar pressure) was used to detect the intensity of the incoming X-ray radiation, and a scintillation counter was used for the transmitted intensity. The goniometer section of the spectrometer was filled with helium buffer gas to avoid the air absorption of X-rays. Ten spectra were acquired and averaged for each sample.

## ■ ASSOCIATED CONTENT

### § Supporting Information

The Supporting Information is available free of charge on the ACS Publications website at DOI: 10.1021/acs.chemmater.9b02074.

Additional XRPD and Rietveld refinement results for the intermediate phases of  $\text{Li}_{2-x}\text{VO}_2\text{F}$  with 12 h immersion in *n*-BuLi. Structural parameters for the intermediate phases. Raman spectra of cycled lithium anode. DEMS measurement for  $\text{Li}_2\text{VO}_2\text{F}$  (PDF)

## ■ AUTHOR INFORMATION

### Corresponding Author

\*E-mail: m.fichtner@kit.edu.

### ORCID

Musa Ali Cambaz: 0000-0002-4249-3486

Bhaghavathi P. Vinayan: 0000-0001-6491-5160

Syed Atif Pervez: 0000-0002-7134-7103

### Notes

The authors declare no competing financial interest.

## ■ ACKNOWLEDGMENTS

Financial support is acknowledged by the FET-OPEN project “LiRichFCC” of the European Commission (grant agreement # 711792). This work contributes to the research performed at CELEST (Center for Electrochemical Energy Storage Ulm-Karlsruhe). The staff at beamline BM01, SNBL/ESRF, is greatly acknowledged for experimental assistance. Rune Johnsen is acknowledged for the measurement at the beamline and the help with the structural characterization. Alexander Schiele and Dr. Torsten Brezesinski are acknowledged for the DEMS measurement. A.A.G. and Y.V.R. acknowledge a grant of the RFBR according to the research project No 17-02-01350\17. S. A. Pervez gratefully acknowledges the financial support by the Alexander von Humboldt Foundation, Bonn, Germany.

## ■ REFERENCES

- (1) Myung, S.-T.; Maglia, F.; Park, K.-J.; Yoon, C. S.; Lamp, P.; Kim, S.-J.; Sun, Y.-K. Nickel-Rich Layered Cathode Materials for Automotive Lithium-Ion Batteries: Achievements and Perspectives. *ACS Energy Lett.* **2017**, 2 (1), 196–223.
- (2) Etacheri, V.; Marom, R.; Elazari, R.; Salitra, G.; Aurbach, D. Challenges in the Development of Advanced Li-Ion Batteries: A Review. *Energy Environ. Sci.* **2011**, 4 (9), 3243.
- (3) Scrosati, B.; Hassoun, J.; Sun, Y.-K. Lithium-Ion Batteries. A Look into the Future. *Energy Environ. Sci.* **2011**, 4 (9), 3287.
- (4) Lee, J.; Urban, A.; Li, X.; Su, D.; Hautier, G.; Ceder, G. Unlocking the Potential of Cation-Disordered Oxides for Rechargeable Lithium Batteries. *Science (Washington, DC, U. S.)* **2014**, 343 (6170), 519–522.
- (5) Yabuuchi, N.; Takeuchi, M.; Nakayama, M.; Shiiba, H.; Ogawa, M.; Nakayama, K.; Ohta, T.; Endo, D.; Ozaki, T.; Inamasu, T.; et al. High-Capacity Electrode Materials for Rechargeable Lithium Batteries:  $\text{Li}_3\text{NbO}_4$ -Based System with Cation-Disordered Rocksalt Structure. *Proc. Natl. Acad. Sci. U. S. A.* **2015**, 112 (25), 7650–7655.
- (6) Lee, J.; Seo, D.-H.; Balasubramanian, M.; Twu, N.; Li, X.; Ceder, G. A New Class of High Capacity Cation-Disordered Oxides for Rechargeable Lithium Batteries: Li–Ni–Ti–Mo Oxides. *Energy Environ. Sci.* **2015**, 8 (11), 3255–3265.
- (7) Hoshino, S.; Glushenkov, A. M.; Ichikawa, S.; Ozaki, T.; Inamasu, T.; Yabuuchi, N. Reversible Three-Electron Redox Reaction



of Mo 3+ /Mo 6+ for Rechargeable Lithium Batteries. *ACS Energy Lett.* **2017**, *2* (4), 733–738.

(8) Kitchaev, D. A.; Lun, Z.; Richards, W. D.; Ji, H.; Clément, R. J.; Balasubramanian, M.; Kwon, D.-H.; Dai, K.; Papp, J. K.; Lei, T.; et al. Design Principles for High Transition Metal Capacity in Disordered Rocksalt Li-Ion Cathodes. *Energy Environ. Sci.* **2018**, *11* (8), 2159–2171.

(9) KITAJOU, A.; TANAKA, K.; MIKI, H.; KOGA, H.; OKAJIMA, T.; OKADA, S. Improvement of Cathode Properties by Lithium Excess in Disordered Rocksalt  $\text{Li}_2 + 2x\text{Mn}1-x\text{Ti}1-x\text{O}_4$ . *Electrochemistry* **2016**, *84* (8), 597–600.

(10) Cambaz, M. A.; Vinayan, B. P.; Euchner, H.; Johnsen, R. E.; Guda, A. A.; Mazilkin, A.; Rusalev, Y. V.; Trigub, A. L.; Gross, A.; Fichtner, M. Design of Nickel-Based Cation-Disordered Rock-Salt Oxides: The Effect of Transition Metal ( $M = \text{V}, \text{Ti}, \text{Zr}$ ) Substitution in  $\text{LiNi}_0.5\text{M}_0.5\text{O}_2$  Binary Systems. *ACS Appl. Mater. Interfaces* **2018**, *10* (26), 21957–21964.

(11) Twu, N.; Li, X.; Urban, A.; Balasubramanian, M.; Lee, J.; Liu, L.; Ceder, G. Designing New Lithium-Excess Cathode Materials from Percolation Theory: Nanohighways in  $\text{Li}_x\text{Ni}_{2-4x/3}\text{Sb}_{x/3}\text{O}_2$ . *Nano Lett.* **2015**, *15* (1), 596–602.

(12) Nakajima, M.; Yabuuchi, N. Lithium-Excess Cation-Disordered Rocksalt-Type Oxide with Nanoscale Phase Segregation:  $\text{Li}_{1.25}\text{Nb}_{0.25}\text{V}_{0.5}\text{O}_2$ . *Chem. Mater.* **2017**, *29* (16), 6927–6935.

(13) Cambaz, M. A.; Vinayan, B. P.; Clemens, O.; Munnangi, A. R.; Chakravadhanula, V. S. K.; Kübel, C.; Fichtner, M. Vanadium Oxyfluoride/Few-Layer Graphene Composite as a High-Performance Cathode Material for Lithium Batteries. *Inorg. Chem.* **2016**, *55* (8), 3789–3796.

(14) Chen, R.; Ren, S.; Knapp, M.; Wang, D.; Witter, R.; Fichtner, M.; Hahn, H. Disordered Lithium-Rich Oxyfluoride as a Stable Host for Enhanced Li + Intercalation Storage. *Adv. Energy Mater.* **2015**, *5* (9), 1401814.

(15) Ren, S.; Chen, R.; Maawad, E.; Dolotko, O.; Guda, A. A.; Shapovalov, V.; Wang, D.; Hahn, H.; Fichtner, M. Improved Voltage and Cycling for Li + Intercalation in High-Capacity Disordered Oxyfluoride Cathodes. *Adv. Sci.* **2015**, *2* (10), 1500128.

(16) Hoshino, S.; Glushenkov, A. M.; Ichikawa, S.; Ozaki, T.; Inamasu, T.; Yabuuchi, N. Reversible Three-Electron Redox Reaction of Mo 3+ /Mo 6+ for Rechargeable Lithium Batteries. *ACS Energy Lett.* **2017**, *2* (4), 733–738.

(17) Richards, W. D.; Dacek, S. T.; Kitchaev, D. A.; Ceder, G. Fluorination of Lithium-Excess Transition Metal Oxide Cathode Materials. *Adv. Energy Mater.* **2018**, *8* (5), 1701533.

(18) Lee, J.; Papp, J. K.; Clément, R. J.; Sallis, S.; Kwon, D.-H.; Shi, T.; Yang, W.; McCloskey, B. D.; Ceder, G. Mitigating Oxygen Loss to Improve the Cycling Performance of High Capacity Cation-Disordered Cathode Materials. *Nat. Commun.* **2017**, *8* (1), 981.

(19) Wang, X.; Huang, Y.; Ji, D.; Omenya, F.; Karki, K.; Sallis, S.; Piper, L. F. J.; Wiaderek, K. M.; Chapman, K. W.; Chernova, N. A.; et al. Structure Evolution and Thermal Stability of High-Energy-Density Li-Ion Battery Cathode  $\text{Li}_2\text{VO}_2\text{F}$ . *J. Electrochem. Soc.* **2017**, *164*, A1552.

(20) Pérez-Flores, J. C.; Villamor, R.; Ávila-Brande, D.; Gallardo Amores, J. M.; Morán, E.; Kuhn, A.; García-Alvarado, F. VO 2 F: A New Transition Metal Oxyfluoride with High Specific Capacity for Li Ion Batteries. *J. Mater. Chem. A* **2015**, *3* (41), 20508–20515.

(21) Chen, R.; Maawad, E.; Knapp, M.; Ren, S.; Beran, P.; Witter, R.; Hempelmann, R. Lithiation-Driven Structural Transition of VO 2 F into Disordered Rock-Salt  $\text{Li}_x\text{VO}_2\text{F}$ . *RSC Adv.* **2016**, *6* (69), 65112–65118.

(22) Wang, X.; Lin, Y.-C.; Zhou, H.; Omenya, F.; Chu, I.-H.; Karki, K.; Sallis, S.; Rana, J.; Piper, L. F. J.; Chernova, N. A.; et al. Structural Changes in a High-Energy Density VO 2 F Cathode upon Heating and Li Cycling. *ACS Appl. Energy Mater.* **2018**, *1* (9), 4514–4521.

(23) Zhang, H.; Feng, W.; Nie, J.; Zhou, Z. Recent Progresses on Electrolytes of Fluorosulfonimide Anions for Improving the Performances of Rechargeable Li and Li-Ion Battery. *J. Fluorine Chem.* **2015**, *174*, 49–61.

(24) Eshetu, G. G.; Grugeon, S.; Gachot, G.; Mathiron, D.; Armand, M.; Laruelle, S. LiFSI vs. LiPF6 Electrolytes in Contact with Lithiated Graphite: Comparing Thermal Stabilities and Identification of Specific SEI-Reinforcing Additives. *Electrochim. Acta* **2013**, *102*, 133–141.

(25) Wang, J.; Yamada, Y.; Sodeyama, K.; Chiang, C. H.; Tateyama, Y.; Yamada, A. Superconcentrated Electrolytes for a High-Voltage Lithium-Ion Battery. *Nat. Commun.* **2016**, *7* (1), 12032.

(26) YAMADA, Y. Developing New Functionalities of Superconcentrated Electrolytes for Lithium-Ion Batteries. *Electrochemistry* **2017**, *85* (9), 559–565.

(27) Golden, J. H.; DiSalvo, F. J.; Frechet, J. M. J. Room-Temperature Synthesis of  $(\text{LiMo}_3\text{Se}_3)_n$  and the Determination of the Relative Reduction Potential of Tert-Butyllithium. *Chem. Mater.* **1994**, *6* (6), 844–849.

(28) Cambaz, M. A.; Vinayan, B. P.; Euchner, H.; Johnsen, R. E.; Guda, A. A.; Mazilkin, A.; Rusalev, Y. V.; Trigub, A. L.; Gross, A.; Fichtner, M. Design of Nickel-Based Cation-Disordered Rock-Salt Oxides: The Effect of Transition Metal ( $M = \text{V}, \text{Ti}, \text{Zr}$ ) Substitution in  $\text{LiNi}_0.5\text{M}_0.5\text{O}_2$  Binary Systems. *ACS Appl. Mater. Interfaces* **2018**, *10* (26), 21957–21964.

(29) Cambaz, M. A.; Vinayan, B. P.; Clemens, O.; Munnangi, A. R.; Chakravadhanula, V. S. K.; Kübel, C.; Fichtner, M. Vanadium Oxyfluoride/Few-Layer Graphene Composite as a High-Performance Cathode Material for Lithium Batteries. *Inorg. Chem.* **2016**, *55* (8), 3789–3796.

(30) Momma, K.; Izumi, F. VESTA 3 for Three-Dimensional Visualization of Crystal, Volumetric and Morphology Data. *J. Appl. Crystallogr.* **2011**, *44* (6), 1272–1276.

(31) Aurbach, D.; Markovsky, B.; Salitra, G.; Markevich, E.; Talyossef, Y.; Koltypin, M.; Nazar, L.; Ellis, B.; Kovacheva, D. Review on Electrode–Electrolyte Solution Interactions, Related to Cathode Materials for Li-Ion Batteries. *J. Power Sources* **2007**, *165* (2), 491–499.

(32) Wang, J.; Yamada, Y.; Sodeyama, K.; Chiang, C. H.; Tateyama, Y.; Yamada, A. Superconcentrated Electrolytes for a High-Voltage Lithium-Ion Battery. *Nat. Commun.* **2016**, *7* (1), 12032.

(33) Qian, J.; Henderson, W. A.; Xu, W.; Bhattacharya, P.; Engelhard, M.; Borodin, O.; Zhang, J.-G. High Rate and Stable Cycling of Lithium Metal Anode. *Nat. Commun.* **2015**, *6* (1), 6362.

(34) Biesinger, M. C.; Lau, L. W. M.; Gerson, A. R.; Smart, R. S. C. Resolving Surface Chemical States in XPS Analysis of First Row Transition Metals, Oxides and Hydroxides: Sc, Ti, V, Cu and Zn. *Appl. Surf. Sci.* **2010**, *257* (3), 887–898.

(35) Lee, S.-H.; Cheong, H. M.; Je Seong, M.; Liu, P.; Tracy, C. E.; Mascarenhas, A.; Pitts, J. R.; Deb, S. K. Microstructure Study of Amorphous Vanadium Oxide Thin Films Using Raman Spectroscopy. *J. Appl. Phys.* **2002**, *92* (4), 1893–1897.

(36) Zhang, C.; Yang, Q.; Koughia, C.; Ye, F.; Sanayei, M.; Wen, S.-J.; Kasap, S. Characterization of Vanadium Oxide Thin Films with Different Stoichiometry Using Raman Spectroscopy. *Thin Solid Films* **2016**, *620*, 64–69.

(37) Yu, X.; Manthiram, A. Electrode–Electrolyte Interfaces in Lithium-Based Batteries. *Energy Environ. Sci.* **2018**, *11* (3), 527–543.

(38) Edström, K.; Gustafsson, T.; Thomas, J. O. The Cathode–Electrolyte Interface in the Li-Ion Battery. *Electrochim. Acta* **2004**, *50* (2–3), 397–403.

(39) Wang, C.; Xing, L.; Vatamanu, J.; Chen, Z.; Lan, G.; Li, W.; Xu, K. Overlooked Electrolyte Destabilization by Manganese (II) in Lithium-Ion Batteries. *Nat. Commun.* **2019**, *10* (1), 3423.

(40) Cabana, J.; Kwon, B. J.; Hu, L. Mechanisms of Degradation and Strategies for the Stabilization of Cathode–Electrolyte Interfaces in Li-Ion Batteries. *Acc. Chem. Res.* **2018**, *51* (2), 299–308.

(41) Chen, D.; Kan, W. H.; Chen, G. Understanding Performance Degradation in Cation-Disordered Rock-Salt Oxide Cathodes. *Adv. Energy Mater.* **2019**, *9* (31), 1901255.

(42) Cambaz, M. A.; Vinayan, B. P.; Geßwein, H.; Schiele, A.; Sarapulova, A.; Diemant, T.; Mazilkin, A.; Brezesinski, T.; Behm, R. J.; Ehrenberg, H.; et al. Oxygen Activity in Li-Rich Disordered Rock-Salt

Oxide and the Influence of LiNbO<sub>3</sub> Surface Modification on the Electrochemical Performance. *Chem. Mater.* **2019**, *31* (12), 4330–4340.

(43) Yamamoto, T. Assignment of Pre-Edge Peaks in K-Edge x-Ray Absorption Spectra of 3d Transition Metal Compounds: Electric Dipole or Quadrupole? *X-Ray Spectrom.* **2008**, *37* (6), 572–584.

(44) Clément, R. J.; Kitchaev, D.; Lee, J.; Gerbrand, C. Short-Range Order and Unusual Modes of Nickel Redox in a Fluorine-Substituted Disordered Rocksalt Oxide Lithium-Ion Cathode. *Chem. Mater.* **2018**, *30* (19), 6945–6956.

(45) Metzger, M.; Strehle, B.; Solchenbach, S.; Gasteiger, H. A. Origin of H<sub>2</sub> Evolution in LIBs: H<sub>2</sub>O Reduction vs. Electrolyte Oxidation. *J. Electrochem. Soc.* **2016**, *163* (5), A798–A809.

(46) Berkes, B. B.; Schiele, A.; Sommer, H.; Brezesinski, T.; Janek, J. On the Gassing Behavior of Lithium-Ion Batteries with NCM523 Cathodes. *J. Solid State Electrochem.* **2016**, *20* (11), 2961–2967.

(47) Metzger, M.; Sicklinger, J.; Haering, D.; Kavakli, C.; Stinner, C.; Marino, C.; Gasteiger, H. A. Carbon Coating Stability on High-Voltage Cathode Materials in H<sub>2</sub>O-Free and H<sub>2</sub>O-Containing Electrolyte. *J. Electrochem. Soc.* **2015**, *162* (7), A1227–A1235.

(48) Berkes, B. B.; Jozwiuk, A.; Vračar, M.; Sommer, H.; Brezesinski, T.; Janek, J. Online Continuous Flow Differential Electrochemical Mass Spectrometry with a Realistic Battery Setup for High-Precision, Long-Term Cycling Tests. *Anal. Chem.* **2015**, *87* (12), 5878–5883.

(49) Hammersley, A. P.; Svensson, S. O.; Hanfland, M.; Fitch, A. N.; Hausermann, D. Two-Dimensional Detector Software: From Real Detector to Idealised Image or Two-Theta Scan. *High Pressure Res.* **1996**, *14* (4–6), 235–248.

(50) Ashiotis, G.; Deschildre, A.; Nawaz, Z.; Wright, J. P.; Karkoulis, D.; Picca, F. E.; Kieffer, J. The Fast Azimuthal Integration Python Library: PyFAI. *J. Appl. Crystallogr.* **2015**, *48* (2), 510–519.